

Dual-Targeted Theranostic Delivery of miRs Arrests Abdominal Aortic Aneurysm Development

Xiaowei Wang,^{1,2,3} Amy Kate Searle,^{1,2,3} Jan David Hohmann,¹ Ao Leo Liu,^{1,2} Meike-Kristin Abraham,¹ Jathushan Palasubramaniam,¹ Bock Lim,¹ Yu Yao,¹ Maria Wallert,¹ Eefang Yu,^{1,2} Yung-Chih Chen,¹ and Karlheinz Peter^{1,2}

¹Atherothrombosis and Vascular Biology, Baker Heart and Diabetes Institute, 75 Commercial Road, Melbourne, VIC 3004, Australia; ²Department of Medicine, Monash University, Melbourne, VIC, Australia

Abdominal aortic aneurysm (AAA) is an often deadly disease without medical, non-invasive treatment options. The upregulation of vascular cell adhesion molecule-1 (VCAM-1) on aortic endothelium provides an early target epitope for a novel biotechnological theranostic approach. MicroRNA-126 was used as a therapeutic agent, based on its capability to downregulate VCAM-1 expression in endothelial cells and thereby reduces leukocyte adhesion and exerts anti-inflammatory effects. Ultrasound microbubbles were chosen as carriers, allowing both molecular imaging as well as targeted therapy of AAA. Microbubbles were coupled with a VCAM-1-targeted single-chain antibody (scFv_{mVCAM-1}) and a microRNA-126 mimic (M₁₂₆) constituting theranostic microbubbles (Targ^{MB}-M₁₂₆). Targ^{MB}-M₁₂₆ downregulates VCAM-1 expression *in vitro* and in an *in vivo* acute inflammatory murine model. Most importantly, using Targ^{MB}-M₁₂₆ and ultrasound-guided burst delivery of M₁₂₆, the development of AAA in an angiotensin-II-induced mouse model can be prevented. Overall, we describe a unique biotechnological theranostic approach with the potential for early diagnosis and long-sought-after medical therapy of AAA.

INTRODUCTION

Abdominal aortic aneurysm (AAA) presents a major cause of sudden, premature death.¹ Patients diagnosed with AAA are typically monitored by regular ultrasound scans. If the diameter of the aorta has reached 5.5 cm, the only effective treatment is surgical or endovascular repair, which is associated with a substantial complication rate.² Despite several clinical trials testing various treatment options, there are currently no secondary prevention measures or non-invasive treatment options available.²

We propose and describe here a novel theranostic approach for early diagnosis and a long-sought-after treatment option for AAA. It combines the use of recombinant antibody-targeted ultrasound microbubbles (MBs) for imaging and ultrasound-burst selective drug delivery, microRNA (miR)-based nucleic acid therapeutics, and the utilization of an endothelial surface protein both as targeting epitope as well as effector molecule for anti-inflammatory therapy.

Vascular cell adhesion molecule-1 (VCAM-1) is an endothelial adhesion molecule that mediates leukocyte adhesion to inflamed endothelial cells (ECs) and is upregulated in vascular diseases, such as atherosclerosis³ and AAA.⁴ VCAM-1 expression has been shown to be regulated by miR-126, which thereby modulates vascular inflammation and integrity.^{5–8} miRs have attracted major interest as therapeutic agents and are currently being tested in multiple clinical trials.⁹ We investigated a miR-126 mimetic (M₁₂₆) as a therapeutic approach to downregulate VCAM-1 expression and ultimately to deliver anti-inflammatory therapy to the area of AAA development.

For AAA diagnosis/imaging, ultrasound is ideal as it is highly mobile, has no side effects, and provides real-time imaging and overall is highly cost-effective. MBs are US Food and Drug Administration (FDA) approved as ultrasound contrast agents and can be used as drug carriers, allowing localized delivery of drugs upon the selective delivery of an ultrasound burst. We have previously shown that MBs can be used for theranostic approaches, e.g., by conjugation with activated platelet-targeted antibodies and fibrinolytic drugs, allowing simultaneous diagnosis and treatment of acute thrombosis.^{10,11}

Undoubtedly, identifying targets for AAA treatment that non-invasively impede upon aneurysmal growth is of great clinical relevance and has inspired recent novel studies.¹² Our approach specifically and non-invasively targets inflamed ECs via a single-chain antibody (scFv) toward VCAM-1. In addition to this scFv-based targeting, ultrasonic bursting provides additional selectivity for transfection of miR-126 mimetics. This unique, dual-targeted

Received 20 November 2017; accepted 11 February 2018;
<https://doi.org/10.1016/j.ymthe.2018.02.010>.

³These authors contributed equally to this work.

Correspondence: Xiaowei Wang, Atherothrombosis and Vascular Biology, Baker Heart and Diabetes Institute, 75 Commercial Road, Melbourne, VIC 3004, Australia.

E-mail: xiaowei.wang@baker.edu.au

Correspondence: Karlheinz Peter, Atherothrombosis and Vascular Biology, Baker Heart and Diabetes Institute, 75 Commercial Road, Melbourne, VIC 3004, Australia.

E-mail: karlheinz.peter@baker.edu.au



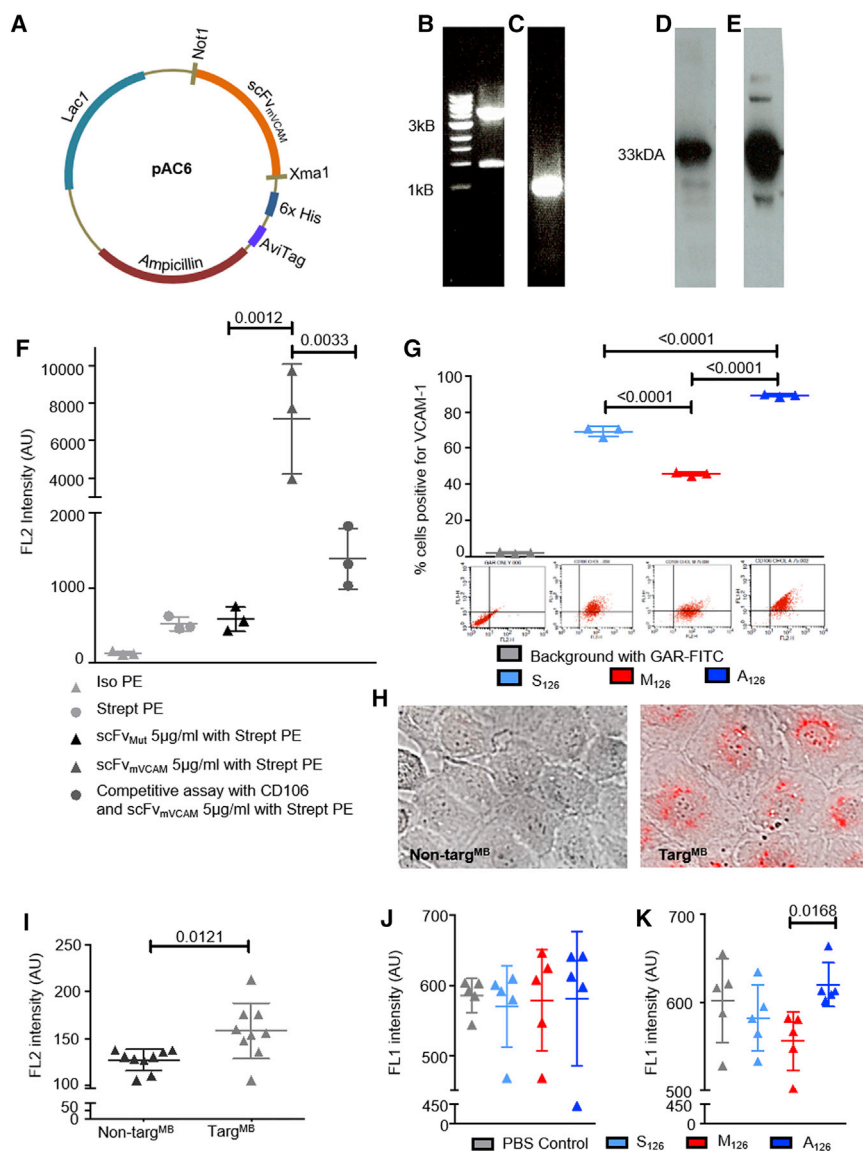


Figure 1. Generation and Functional Evaluation of scFv_{mVCAM-1}, miR-126 Constructs, and Targ^{MB}

(A) Gene map of scFv_{mVCAM-1} construct in pAC6 vector. (B) Electrophoresis of pAC6 plasmid (above 3 kDa marker) after restriction digest is shown; successful enzymatic digestion is observed with visualization of 1-kB cut out. (C) Electrophoresis of scFv_{mVCAM-1} (around 1 kDa marker) after PCR amplification is shown. (D and E) Western blot analysis (D) shows successful protein purification of scFv_{mVCAM-1} demonstrated with horseradish peroxidase (HRP)-coupled anti-6× His-tag antibody, and *in vivo* biotinylation of scFv_{mVCAM-1} (E) demonstrated with streptavidin-HRP; both western blots show bands around 33 kDa. (F) Functionality of scFv_{mVCAM-1} and efficiency of *in vivo* biotinylation were evaluated with R-phycoerythrin streptavidin via flow cytometry; specificity of scFv_{mVCAM-1} (5 μg/mL)-targeting VCAM-1 was demonstrated in a competitive assay, using commercially available CD106 and scFv_{mVCAM-1} (n = 3). (G) Flow cytometry assays evaluated effect of miR-126 constructs on VCAM-1 expression; assays demonstrate increased VCAM-1 expression on SVEC4-10 cells after transfection with A₁₂₆ and decreased expression with M₁₂₆ as compared to those with S₁₂₆ (n = 3). Representative flow cytometry dot plots are shown below each bar graph. (H) Representative images show successful transfection of miR-126 using Targ^{MB} via microscopy using bright field and TRITC fluorescence channel; scale bar = 10 μm. (I) Flow cytometry analysis detected Cy3 (on miR) after transfection into SVEC4-10 cells (n = 9). (J) Flow cytometry assays show no change in VCAM-1 expression when non-Targ^{MB} was used for transfection of miR-126. (K) Flow cytometry assays show decreased expression of VCAM-1 after transfection with Targ^{MB}-M₁₂₆ as compared to Targ^{MB}-A₁₂₆ (n = 5); assays with two groups were analyzed using Student's t tests and those with more than two groups with equal numbers using repeated-measures one-way ANOVA with Bonferroni post tests.

delivery system is well suited to provide a high therapeutic payload directly to the site of inflamed endothelium at the AAA.

Overall, the presented combination of molecular imaging of AAA and targeted drug delivery approach holds immense potential for clinical translation in a disease with limited therapeutic options and often fatal outcome.

RESULTS AND DISCUSSION

To allow targeting of MBs, a single-chain antibody targeting mouse VCAM-1 (scFv_{mVCAM-1})¹³ was adapted for MB conjugation by subcloning into the pAC6 vector system, consisting of a C-terminal AviTag, which enables *in vivo* biotinylation during protein production (Figure 1A). DNA amplification and restriction digest were evaluated by electrophoresis (Figures 1B and 1C), and production of the adapted

scFv_{mVCAM-1} was confirmed by western blotting (Figures 1D and 1E). The non-binding control (scFv_{Mut}) was generated previously.¹⁴

Mouse VCAM-1-expressing *Mus musculus* axillary lymph node/vascular epithelium (SVEC4-10) cells were used to confirm the binding specificity of scFv_{mVCAM-1}. Binding of commercially available anti-CD106 together with a goat-anti-rat-fluorescein-isothiocyanate (GAR-FITC) secondary antibody confirmed VCAM-1 expression on SVEC4-10 cells, whereas no binding was observed for the isotype FITC control or GAR-FITC secondary antibody (Figure S1A). Fluorescence intensity in the SVEC4-10 cells was increased using biotinylated scFv_{mVCAM-1} with R-phycoerythrin (PE) streptavidin as compared to controls (Figure 1F). Competitive binding between anti-CD106 and scFv_{mVCAM-1} confirmed the specificity of scFv_{mVCAM-1} (Figure 1F).

Three different cholesterol- (for attachment to MBs and transfer through the cell membrane) and fluorescence-tagged miR-126 oligos were used: (1) anti-miR-126 (A_{126}), which induces VCAM-1 expression; (2) mimic-miR-126 (M_{126}), which represses VCAM-1 expression; and (3) scrambled-miR-126 (S_{126}) as control. Changes in VCAM-1 expression were assessed after the respective transfection into SVEC4-10 cells using qRT-PCR and flow cytometry. We observed increased VCAM-1 expression using A_{126} and decreased expression with M_{126} as compared to S_{126} (Figure S1C). Similarly, flow cytometry assays demonstrated significantly more VCAM-1 expression with A_{126} -transfected SVEC4-10 cells and less with M_{126} , as compared to those with S_{126} (Figure 1G).

MBs were first conjugated with either scFv_{mVCAM-1} (Targ^{MB}) or non-binding scFv_{Mut} (non-Targ^{MB}), followed by incubation with the fluorescence-tagged miR therapeutics. The 3' cholesterol tag has been proven to increase the binding capacity of the miRs to MBs¹⁵; however, it is yet to be investigated how long these bonds are stable *in vivo* in the presence of other hydrophilic blood components. For additional selectivity of our miR therapeutics, we employed an ultrasonic drug delivery approach using ultrasound bursts. After incubation of Targ^{MB}-miR with SVEC4-10 cells and washing, we burst the Targ^{MB}-miR to deliver the Cy3-tagged miR. Fluorescence was visible in the nuclei of cells incubated with Targ^{MB}-miR, but not with the non-Targ^{MB}-miR (Figures 1H and S1B). Similar results were demonstrated on flow cytometry (Figure 1I).

Following the promising results of our dual-targeting and ultrasonic drug delivery, we investigated whether the expression of VCAM-1 on SVEC4-10 cells could be altered using this approach. Flow cytometry results showed no alteration in VCAM-1 expression of SVEC4-10 cells post-transfection with non-Targ^{MB}- A_{126} , non-Targ^{MB}- M_{126} , non-Targ^{MB}- S_{126} , or non-Targ^{MB} alone as controls (Figure 1J). Similarly, no differences in VCAM-1 expression were observed post-transfection using just Targ^{MB} alone as control or Targ^{MB}- S_{126} (Figure 1K). However, a significant decrease in VCAM-1 expression was seen in cells transfected using Targ^{MB}- M_{126} as compared to Targ^{MB}- A_{126} (Figure 1K), demonstrating the specific targeting ability of our scFv_{mVCAM-1} and successful ultrasonic drug delivery, which resulted in successful modulation of VCAM-1 expression.

As a first *in vivo* proof of concept, we validated the efficiency and effectiveness of our Targ^{MB}- M_{126} using a murine model of acute inflammation intraperitoneal (i.p.) injection of lipopolysaccharide (LPS). Mice were then randomized before being treated with Targ^{MB}- M_{126} , Targ^{MB}- A_{126} , or Targ^{MB}- S_{126} . After 5 min, ultrasound bursts were applied to the abdominal and thoracic aorta. Using qRT-PCR, we observed decreased VCAM-1 gene expression of the thoracic aorta in animals treated with Targ^{MB}- M_{126} and increased expression in those treated with Targ^{MB}- A_{126} compared to Targ^{MB}- S_{126} (Figure 2B). Immunohistochemistry using goat-anti-mouse VCAM-1 polyclonal (GAM-VCAM-1) antibody also showed decreased VCAM-1 expression in animals treated with Targ^{MB}- M_{126} as compared to those treated with Targ^{MB}- A_{126} or Targ^{MB}- S_{126} (Figure 2A).

Following the promising results from the *in vivo* acute inflammation model, we investigated our targeted theranostic approach for the prevention/treatment of aneurysm severity in an angiotensin (Ang)-II-induced AAA murine model (Figure 2C). Ultrasound monitoring of the abdominal aorta showed an increase in the suprarenal (pre-renal) diameter 1 week post-Ang-II induction for all treatment groups and a slight increase in the infrarenal (post-renal) diameter, as compared to baseline measurements (Figure S2). In order to determine the diagnostic capability of the Targ^{MB} on the abdominal aorta wall, we measured the contrast intensity both before and 20 min post-injection. A significant difference in contrast intensity was observed in the Ang-II-induced AAA animals, 20 min after the injection of Targ^{MB}, demonstrating that our unique VCAM-1-targeted MBs can bind directly at the site of inflamed ECs where AAA develops (Figure 2D). No increase in contrast intensity was seen in healthy PBS control mice (Figure 2E).

We then utilized our theranostic approach of Targ^{MB} loaded with miRs to investigate the impact of Targ^{MB}- M_{126} upon aneurysm severity. Weekly intravenous injection, ultrasound imaging, and ultrasonic bursting (abdominal aorta, both suprarenal and infrarenal) were performed. Ultrasound measurements of the abdominal aorta 4 weeks post-treatment showed a greater difference in vessel diameter (compared to baseline before disease induction) for animals treated with Targ^{MB}- A_{126} or Targ^{MB}- S_{126} as compared to those treated with Targ^{MB}- M_{126} (Figures 2F and 2G). At week 4, 3D ultrasound reconstruction of the abdominal aorta showed massive areas of plaque buildup and aneurysm in animals treated with Targ^{MB}- A_{126} or Targ^{MB}- S_{126} , but not in those treated with Targ^{MB}- M_{126} (Figure 3A; Movies S1, S2, and S3). These results were further confirmed macroscopically on vessel isolation (Figure 3B). Furthermore, immunohistochemistry using GAM-VCAM-1 antibody confirmed the decreased VCAM-1 expression for animals treated with Targ^{MB}- M_{126} as compared to those treated with Targ^{MB}- A_{126} or Targ^{MB}- S_{126} (Figure 3C). Martius Scarlet Blue (MSB) staining also showed plaque buildup and aneurysm in the abdominal aortas of animals treated with Targ^{MB}- A_{126} or Targ^{MB}- S_{126} , whereas very little plaque buildup was observed with Targ^{MB}- M_{126} (Figure 3D).

Ultrasound imaging for the anatomical diagnosis and monitoring of AAA is well established in clinical practice. This study extends the use of ultrasound in AAA toward a unique theranostic application, which allows simultaneous diagnosis and therapy of AAA. We demonstrate that MBs can be used as functional ultrasound contrast agents to assess the inflammatory state of the endothelium, as well as for targeted delivery of therapeutic anti-inflammatory drugs. The targeted delivery of miRs is achieved by conjugating a scFv, which specifically binds to mouse VCAM-1, onto MBs, thereby increasing the therapeutic payload and allowing targeted drug delivery specifically at the site of AAA. We cannot exclude the possibility that there might be free cholesterol-tagged miRs present in the blood stream, which could also be transferred into the cells within the area of disease, potentially facilitated by the ultrasound destruction of our targeted MBs. However, our study demonstrates that the anti-miR-126,

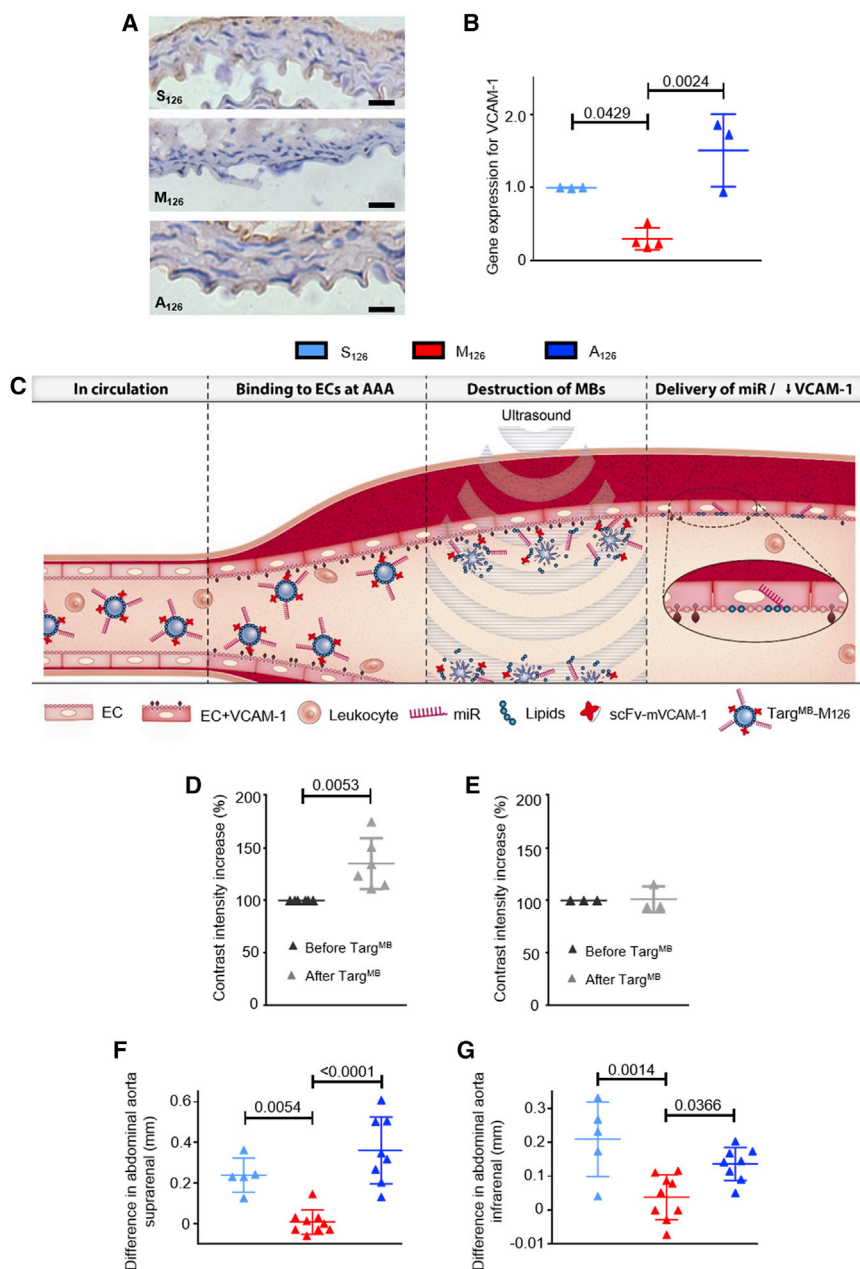


Figure 2. Demonstration of $Targ^{MB}$ -miR Effect on VCAM-1 Expression in Acute Inflammatory Murine Model, $Targ^{MB}$ Binding to Abdominal Aorta of Ang-II-Induced AAA Animals, and Successful Targeted Delivery of miR-126 to Site of Disease

(A) Representative images from immunohistochemistry using goat-anti-mouse VCAM-1 polyclonal antibody show decreased VCAM-1 expression for animals treated with $Targ^{MB}$ - M_{126} as compared to those treated with $Targ^{MB}$ - A_{126} or $Targ^{MB}$ - S_{126} in LPS model of acute inflammation; scale bar = 50 μm . (B) In the same model, VCAM-1 expression on the thoracic aorta assessed via qRT-PCR demonstrates decreased expression in animals treated with $Targ^{MB}$ - M_{126} and increased expression in animals treated with $Targ^{MB}$ - A_{126} ($n = 3-4$); for qRT-PCR assays, ratio of gene expression for animals treated with $Targ^{MB}$ - S_{126} was set to 1. (C) Mechanism of action of double-selective $Targ^{MB}$ -miR therapy in AAA is shown. (D and E) Increased contrast intensity on molecular ultrasound imaging demonstrates (D) successful binding of $Targ^{MB}$ to the inflamed abdominal aorta of mice with Ang-II-induced AAA and (E) no change in healthy mice used as a control ($n = 3-6$). Ultrasound analysis of the abdominal aorta was measured 4 weeks post-treatment. The difference in diameter (from the baseline before disease induction) was calculated. (F and G) A significant increase in the diameter of the (F) supranrenal and (G) infrarenal abdominal aorta was observed in animals treated with $Targ^{MB}$ - A_{126} and $Targ^{MB}$ - S_{126} , whereas the diameter of $Targ^{MB}$ - M_{126} was preserved ($n = 5$ [S_{126}], $n = 9$ [M_{126}], $n = 8$ [A_{126}]). Assays with two groups were analyzed using Student's t tests, and those with more than two groups using ordinary one-way ANOVA with Bonferroni post tests.

this novel therapeutic approach. These data provide proof of concept for a novel, non-invasive, and risk-free theranostic strategy (Figure S3) that allows monitoring and holds great potential to ultimately prevent aneurysmal growth of the abdominal aorta.

We used scFvs for targeting of our MBs because they have major advantages over traditional antibodies. ScFvs are small antibody fragments lacking the Fc region and therefore are minimally immunogenic.¹⁶ In addition, scFvs allow optimization via molecular biology methods, including fusion with drugs,^{14,17} as well as incorporation of specific tags and sequences for purification, bioconjugation, and imaging.¹⁸ Our group has developed several highly specific scFvs for diagnostic imaging,^{14,19-21} targeted therapy,^{17,22-24} and theranostic approaches.¹⁰

$Targ^{MB}$ - A_{126} increases VCAM-1 expression and further aggravates AAA, whereas treatment with a mimic of miR-126, $Targ^{MB}$ - M_{126} , downregulates VCAM-1 expression on the intraluminal surface of the aneurysmal area and effectively prevents the development of AAA. To the best of our knowledge, this is the first study to present targeted theranostic MBs for the therapeutic delivery of miRs in an AAA model. Our targeting approach is specific for areas with VCAM-1 expression, thereby allowing the miR therapeutics to be delivered directly to the area of interest. The use of molecular ultrasound technology to destroy the MBs bound to the wall of the inflamed aorta and to release the miR therapeutics enhances the specificity of

Pioneering studies have analyzed the circulating levels of vascular and inflammation-associated miRs in atherosclerosis,²⁵ acute myocardial infarction,²⁶ and AAA.²⁷⁻²⁹ In particular, one such miR that has been found to be upregulated in AAA is the endothelium-related

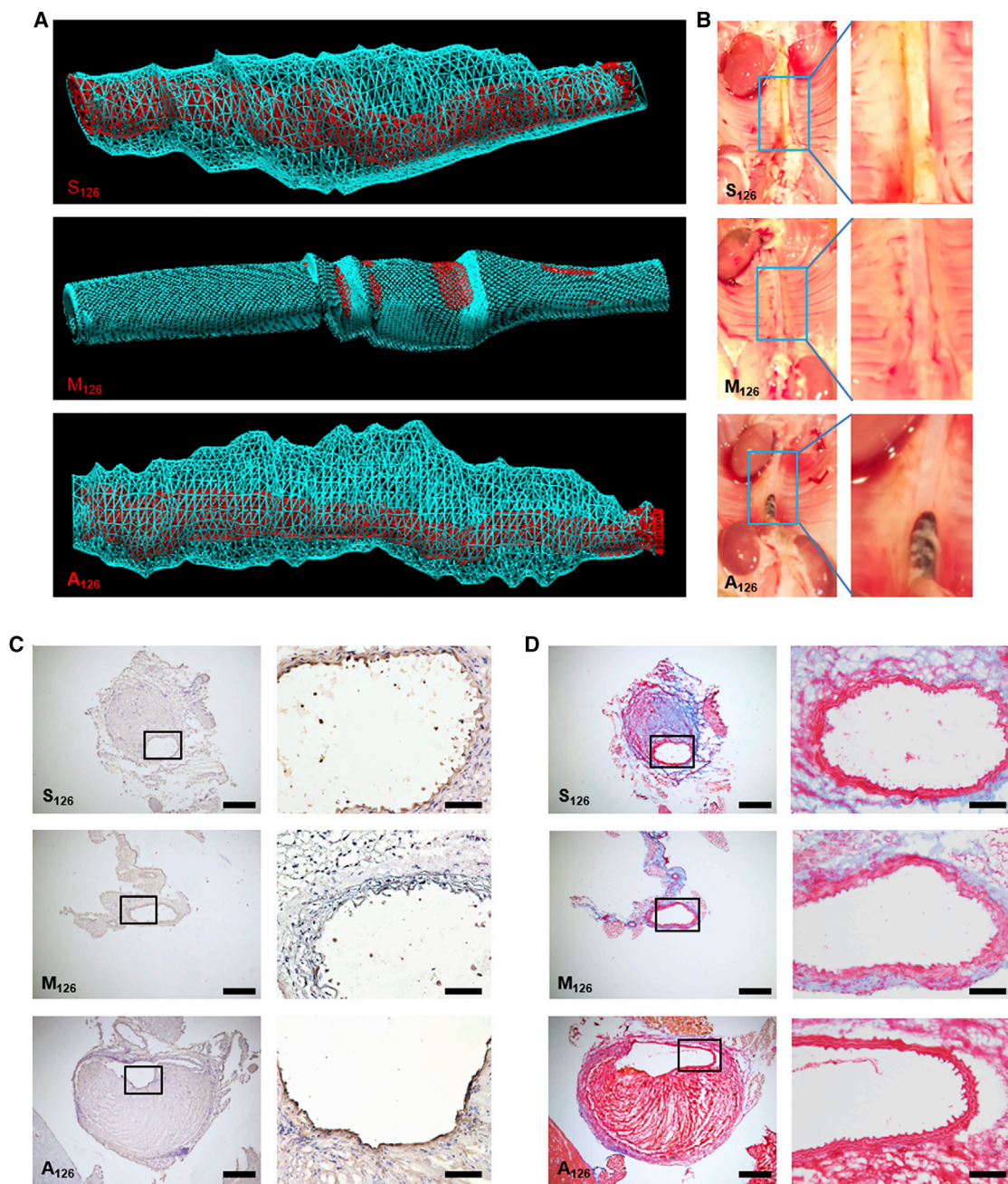


Figure 3. Representative Images of Three-Dimensional Ultrasound Reconstructions of Abdominal Aorta, Photographs of Vessel Isolations, Immunohistochemistry, and Martius Scarlet Blue Demonstrate Profound Effect of VCAM-1-Targeted miR-Carrying Microbubbles

(A) 3D ultrasound reconstruction of abdominal aorta shows vessel lumen (in red), as well as massive areas of plaque buildup and aneurysm (in blue), from animals treated with Targ^{MB}-A₁₂₆ or Targ^{MB}-S₁₂₆, but not in animals treated with Targ^{MB}-M₁₂₆. (B) Vessel isolation shows clean abdominal aorta in mice treated with Targ^{MB}-M₁₂₆ but plaque buildup and aneurysms in mice given Targ^{MB}-S₁₂₆ or Targ^{MB}-A₁₂₆. (C) Immunohistochemistry confirmed a decrease in VCAM-1 expression for Targ^{MB}-M₁₂₆-treated animals as compared to those treated with Targ^{MB}-A₁₂₆ or Targ^{MB}-S₁₂₆. (D) Martius Scarlet Blue showed plaque buildup and aneurysm in abdominal arteries of Targ^{MB}-A₁₂₆- or Targ^{MB}-S₁₂₆-treated animals, whereas very little plaque buildup was observed in Targ^{MB}-M₁₂₆-treated mice.

miR-126.²⁹ Therapeutic miR approaches have attracted major interest, with both pre-clinical and clinical reports describing their immense potential to regulate specific gene expression in a broad

range of diseases.⁹ Several miR-based therapies have been assessed in AAA, such as targeting miR-21, miR-29, miR-181, miR-205, and miR-712.^{30–33} Within the setting of AAA, dysregulation of ECs

augments localized inflammation and expression of integrins and adhesion molecules on the endothelial luminal surface, consequently increasing leukocyte attachment, rolling, and ultimately migration/infiltration into the intimal layer.^{4,5,28} MiR-126 is understood to be exclusive to ECs and therefore has been identified as a crucial endogenous mediator of vascular integrity and angiogenesis and regulator of adhesion molecules.⁵⁻⁷ Our *in vitro* work also highlights the use of M₁₂₆ for the suppression of VCAM-1 expression, and the opposite has been observed using A₁₂₆.

A recent study provided compelling evidence of miR-126's anti-inflammatory effects via increased localized enrichment of CXCL12 following apoptotic microparticle blebbing from ECs, of which miR-126 is a major constituent.³⁴ This study also showed that miR-126 therapy via delivery of endothelial apoptotic bodies decreased overall atherosclerotic lesion size in mouse models of atherosclerosis,³⁴ further validating a role for miR-126 in disease models of endothelial dysfunction and inflammation. Our acute inflammatory model shows that targeted delivery of miR-126 can alter VCAM-1 expression on the thoracic and abdominal aorta of LPS-treated mice.

Based on the presented *in vivo* data, the clinical translation of our targeted theranostic approach appears highly promising for patients with AAA. The VCAM-1-targeting MBs enrich the miR therapeutics at the site of activated ECs, and together with the localized application of an ultrasound burst, non-specific uptake of miR therapeutics in other cell types can be minimized. Overall, the presented theranostic approach has the potential to provide a long-sought-after medical treatment option for patients with AAA.

MATERIALS AND METHODS

Generation of Anti-mVCAM-1 Single-Chain Antibody Containing an AviTag Motif at the C Terminus

The generation of the scFv_{mVCAM-1} has been described previously and was a gift from Prof. Claudia Gottstein.¹³ The scFv_{mVCAM-1} was subcloned into the pAC6 vector system (Avidity, Aurora, CO), which consists of the AviTag motif at the C-terminal. PCR was performed with a sense primer that anneals at the beginning of the scFv sequence and an antisense primer that anneals directly to the 6× His-tag region at the end of the scFv. The following primers were used for PCR: sense strand: 5'-CAG CCG GCC ATG GCG CAG GTT CA-3' and antisense strand: 5'-TCA GAT CCC GGG TAA TGG TGA TGG TGA TGA TG-3'. The antisense strand includes the *Xma*I restriction site. After amplification by PCR, the constructs were then digested with the restriction enzymes *Not*I and *Xma*I (both New England Biolabs, Ipswich, MA) and cloned into pAC6. Electrophoresis on a 0.8% agarose gel with SYBR Safe DNA gel stain (Invitrogen, Carlsbad, CA) was utilized to analyze amplifications of DNA by PCR and restriction digests. Ligation of the plasmids was performed with T4 ligase (NEB, Ipswich, MA) at 16°C overnight. The resulting plasmid constructs were then transformed into Turbo competent *E. coli* cells (NEB, Ipswich, MA). The transformed cells were grown in Luria-Bertani (LB) media containing 100 µg/mL ampicillin and 100 mM glucose at 37°C, and the plasmids were purified using a Plasmid

Mini-Prep Kit (QIAGEN, Hilden, Germany). The respective plasmids were analyzed by electrophoresis on a 0.8% agarose gel with SYBR green, and constructs were confirmed by DNA sequencing. The DNA was then transformed into electrocompetent cell EVB101 (Avidity, Aurora, CO) by electroporation with Bio-Rad Gene Pulser. All agarose gels were visualized using a Bio-Rad Gel-Doc system with Quantity One software (Bio-Rad, Hercules, CA).

Expression, *In Vivo* Biotinylation, and Purification of scFv_{mVCAM-1}-AviTag Construct

Bacterial strains of *E. coli* harboring the plasmid pAC6-scFv_{mVCAM-1}-AviTag were used to inoculate 5 mL of trytone-HEPES-yeast (THY) media containing 10 µg/mL chloramphenicol and 100 µg/mL ampicillin at 37°C.¹⁴ After culturing overnight, 5 mL of the overnight culture was transferred into 1 L of THY media containing 100 µg/mL ampicillin in a non-baffled Erlenmeyer flask. Glucose was added to the THY media to 0.5% final concentration. *In vivo* biotinylation was induced by 50 mM Biotin-D, 50 mM bicine, and 1.5 mM isopropyl β-D-thiogalactoside, when the optical density 600 (OD₆₀₀) of the culture reached 0.7 units. After 3 hr induction, the cells were spun down and resuspended in BugBuster Master Mix (Novagen, Darmstadt, Germany). The cell debris was spun down, and the inclusion bodies were used for protein extraction via 8 M urea. All purified single-chain antibodies carry a 6× His-tag at the C-terminal end of their amino acid sequence for purification by immobilized metal affinity chromatography (IMAC) or for fluorescence-activated cell sorting (FACS) analysis. Proteins were purified with a nickel-based metal affinity chromatography column, Ni-NTA column (Invitrogen, Carlsbad, CA), according to the manufacturer's instruction manual. Fractions of 1 mL were collected and dialyzed against 6 M urea, decreasing slowly in 2 M increments until PBS.

Evaluation of Purity and Efficiency of the *In Vivo* Biotinylation of the scFv_{mVCAM-1}-AviTag Construct

The purity of the proteins and the efficiency of *in vivo* biotinylation were analyzed by western blotting. 30 µL of each purified protein and 6 µL of 5× reducing SDS loading buffer were added to 1.5-mL tubes and denatured at 96°C for 5 min. The samples were run on SDS-PAGE gel in SDS running buffer at 100 V for 2 hr. The gel was then used for western blotting at 100 V for 1 hr 30 min. The membrane was blocked with 1% BSA and hybridized with a specific horseradish peroxidase (HRP). Anti-6× His-tag antibody HRP was used to detect the protein construct, and streptavidin-HRP (BD Biosciences, San Jose, CA) was used to determine the success of the *in vivo* biotinylation of the protein construct. Secondary hybridization was performed with SuperSignal West Pico chemiluminescent substrate (Thermo Scientific, Waltham, MA), an enhanced chemiluminescent (ECL) substrate for the HRP enzyme.

Cholesterol-Tagged miRNA

The sequences of the miR-126 are as follows: mimic-miR-126 (M₁₂₆) 5'-UCG UAC CGU GAG UAA UAA UGC G-3'; anti-miR-126 (A₁₂₆) 5'-CGC ATT ATT ACT CAC GGT ACG A-3'; and scramble-miR-126 (S₁₂₆) 5'-CGC UCA UUC UGC CGG UUG

UUA UG-3'. All miRs were modified with 2-O-methyl, 5'-Cy3, and 3'-cholesterol (VBC Biotech Services, Vienna, Austria).

mVCAM-Expressing SVEC4-10 Cell Culture

SVEC4-10 mice endothelial cells (ATCC, Manassas, VA) were cultured in DMEM (Invitrogen, Carlsbad, CA), supplemented with 1% penicillin/streptomycin, 1% L-glutamine (200 mM), and 10% fetal calf serum to the media (Gibco, Waltham, MA). When the monolayer adherent SVEC4-10 cells reached confluency of 90%, a dissociation reagent containing 0.05% trypsin-EDTA (Gibco, Waltham, MA) was used to detach the cells into a suspension.

Flow Cytometry

SVEC4-10 cells were incubated with 10 $\mu\text{g}/\text{mL}$ of purified scFv_{mVCAM-1} for 10 min at 37°C followed by Penta-His AlexaFluor 488 conjugate (QIAGEN, Hilden, Germany) or R-phycoerythrin streptavidin (Jackson ImmunoResearch Laboratories, West Grove, PA) for 15 min. As a positive control and to determine the VCAM expression, the cells were incubated with CD106 (anti-VCAM) rat-anti-mouse antibody for 10 min at 37°C followed by a goat-anti-rat FITC (GAR-FITC) secondary antibody for 15 min. Samples were fixed with 1 \times Cellfix (BD Biosciences, San Jose, CA) and analyzed by FACS Calibur (BD Biosciences, San Jose, CA). The cell population was distinguished using the forward and sideward light scatter profile. A gate was set around the cell population, and 10,000 cells were analyzed. For determination of VCAM-1 expression, single staining using CD106 and GAR-FITC secondary antibody was used. For determination of miR-126 transfection, the Cy3 on the 5' of the oligo was used.

qPCR for Gene Expression

For *in vitro* work, the total RNA was extracted using Trizol reagent (Invitrogen, Carlsbad, CA) under RNase-free conditions. A DNA Reverse Transcription Kit (Applied Biosystems, Foster City, CA) was used to obtain cDNA from the total RNA samples, according to the manufacturer's instructions. qRT-PCR of miR was carried out using a TaqMan Reverse Transcription Kit (Applied Biosystems, Foster City, CA), according to the manufacturer's instructions. For *in vivo* work, total RNA was extracted using a fibrous tissue isolation kit (QIAGEN, Hilden, Germany) under RNase-free conditions as per the manufacturer's instructions. Initially, two-step qRT-PCR was performed using identical reagents as mentioned previously; however, low yields of RNA on account of the small sample size of the thoracic aorta led to the use of a one-step QuantiFast SYBR green qRT-PCR kit (QIAGEN, Hilden, Germany) for all further assays. All samples were performed in triplicate. The expression levels of VCAM-1 were calculated by the delta-delta Ct method using GAPDH as an internal control.

Preparation of Microbubbles

VisualSonics Target-Ready MBs (8.4×10^8 MBs; VisualSonics, Toronto, Canada) were resuspended in 1 mL sterile saline (0.9% sodium chloride) according to the manufacturer's instructions. 20 μg of scFv_{mVCAM-1} or a non-binding scFv_{Mut} were added to each milliliter

of MBs to generate Targ^{MB} or non-Targ^{MB} as control, respectively, and incubated at room temperature for 20 min. The average radius of a MB is around 1.5 μm , and MBs bear an average of 7,600 streptavidin molecules per μm^2 MB surface, resulting in approximately 6,000 biotinylated scFv molecules per μm^2 of the MB. Targ^{MB} or non-Targ^{MB} was incubated with 100 $\mu\text{g}/\text{mL}$ of one of the three cholesterol-tagged miRs: M₁₂₆; A₁₂₆; or S₁₂₆. This creates 1 molecule of cholesterol-miR to every 200 lipids on the MBs. The following terms are used for this manuscript: Targ^{MB}-M₁₂₆ (VCAM-1-targeted MBs with mimic-miR-126); Targ^{MB}-A₁₂₆ (VCAM-1-targeted MBs with anti-miR-126); and Targ^{MB}-S₁₂₆ (VCAM-1-targeted MBs with scramble-miR-126). For *in vitro* experiments, 10 μL of MB, containing 0.2 μg of scFv and 100 ng of miR, were used. For *in vivo* experiments, 100 μL of MB, containing 2 μg of scFv and 10 μg of miR, were given to each animal per injection.

Ultrasound Burst for Targeted Transfection of miR-126 Using VCAM-1-Targeted Microbubbles Loaded with miR-126

SVEC4-10 cells were seeded into 35 \times 10 mm Petri dishes (Sarstedt, Neumbrecht, Germany) and incubated to allow attachment overnight. Petri dishes were carefully filled with PBS with calcium and magnesium to the brim and taped shut using Parafilm M (Bemis, Neenah, WI). The Targ^{MB}-M₁₂₆, Targ^{MB}-A₁₂₆, or Targ^{MB}-S₁₂₆ was injected using a 30 G needle into the Petri dishes through the Parafilm M. The Petri dishes were placed with the bottom facing up and were gently shaken for 5 min. A washing step was performed to remove unbound MBs before ultrasound bursting was employed to destroy the bound MBs and enable the miR to enter the cells. For washing, the Parafilm M was removed, the supernatant was discarded, and fresh media were added. Ultrasound was performed on the cells using color Doppler mode for 30 s per field of view (4 fields of view per Petri dish) to destroy the MBs. Cells were incubated for 48 hr before microscopy.

In Vivo Mouse Experiments

Male C57BL/6 mice or apolipoprotein E knockout (Apo E^{-/-}) mice were obtained from the Alfred Medical Research and Education Precinct Animal Services and assigned randomly to one of the three groups. Animals were injected with Targ^{MB}-M₁₂₆, Targ^{MB}-A₁₂₆, or Targ^{MB}-S₁₂₆. All experiments involving animals were approved by the Alfred Medical Research and Education Precinct Animal Ethics Committee (E/1406/2013/B and E/1187/2012/B).

The animals were anesthetized using 1.5%–2% isoflurane. Breathing of the animals was monitored to determine the amount of anesthetics used. For animals undergoing ultrasound, the fur was removed by shaving cream (Dove, Sydney, Australia). Mice were placed on a 37°C heated mat to prevent hypothermia.

Acute Inflammatory Mouse Model

Male C57BL/6 mice, 6 to 7 weeks of age (20–25 g), were used for this model. Animals were given an i.p. injection of 50 μg LPS diluted to 100 μL with PBS with calcium and magnesium. 18 hr post-injection, the animals were anesthetized using 1.5%–2% isoflurane and placed on the VisualSonics imaging station. The animals were assigned

randomly to one of the three groups, and Targ^{MB}-M₁₂₆, Targ^{MB}-A₁₂₆, or Targ^{MB}-S₁₂₆ was injected via the tail vein. After 5 min of circulation, we used the burst mode on the Vevo2100 high-frequency small-animal ultrasound scanner and burst the MBs that were attached on the thoracic and abdominal aorta. 48 hr post-ultrasound, the abdominal aorta and the thoracic aorta of the animals were removed for histology and qRT-PCR, respectively.

AAA Mouse Model

Male ApoE^{-/-} mice, 24 weeks of age, were used for this model. The animals were anesthetized using 1.5%–2% isoflurane and placed on a heated mat. A small incision was made in the skin between the scapulae. The connective tissue was carefully spread to create a pocket for an osmotic pump (model 2004, Alzet, Cupertino, CA). A pump containing Ang-II (1,000 ng/kg/min, Sigma, St. Louis, MO) was implanted subcutaneously on the back of the mouse, with the flow mediator pointing away from the incision. The incision was closed using 6-0 fiber suture (Ethicon, Somerville, NJ). The animals were checked extensively over the next 7 days. One week post-pump implantation, the animals were assigned randomly to one of three groups, and Targ^{MB}-M₁₂₆, Targ^{MB}-A₁₂₆, or Targ^{MB}-S₁₂₆ was injected via the tail vein. After 5 min of circulation, we used the burst mode on the Vevo2100 high-frequency small-animal ultrasound scanner and burst the MBs that were attached on the thoracic and abdominal aorta. The injection of the respective treatments was repeated for week 2 and week 3. At week 4, the abdominal aorta and the thoracic aorta of the animals were removed for histology and qRT-PCR, respectively.

In Vivo Ultrasound Molecular Imaging

Ultrasound imaging was performed using a Vevo2100 small-animal high-resolution imaging scanner (VisualSonics, Toronto, Canada) using a 22- to 55-MHz high-frequency transducer (lateral resolution, 100 μm; transverse resolution, 40 μm; focal length, 10 mm; low acoustic pressure or mechanical index, 0.14). The animals were anesthetized using 1.5%–2% isoflurane and placed on the imaging station. Fur was removed by shaving with cream (Dove, Sydney, Australia). For imaging of the abdominal aorta, the transducer was placed directly over the abdomen of the mouse, with the transducer marker facing 12 o'clock. All anatomical imaging was performed in fundamental brightness mode (B mode) using transmit power, 100%; dynamic range, 65 dB. We ensured that the region of interest (abdominal aorta and the branches of the renal arteries) was well visualized via imaging. The diameter of the abdominal aorta was measured both suprarenal (above the renal arteries) and infrarenal (below the renal arteries). The position of the renal arteries ensures that the measurements were repeatedly performed at the same area weekly and therefore ensures its repeatability. For contrast imaging and ultrasonic burst, we used a 13- to 24-MHz high-frequency non-linear contrast transducer. The animals were assigned randomly to one of the three groups, and Targ^{MB}-M₁₂₆, Targ^{MB}-A₁₂₆, or Targ^{MB}-S₁₂₆ was injected via the tail vein. Upon the injection of MBs, we imaged using the nonlinear contrast mode (using transmit power, 10% and dynamic range, 40 dB). After 5 min of circulation, we used the burst mode on the Vevo2100 ultrasound scanner to burst the MBs that were

attached on the thoracic and abdominal aorta. When we employed the burst mode to destroy the MBs, we use a continuous 10-MHz high-power destructive pulse (using transmit power, 100%; high mechanical index, ~0.63; average power, ~0.0676 W/cm²) applied for 2 s every 10 s, which destroys the MBs within the beam elevation. During the burst mode, the transducer is mechanically moved to cover the desired target area. 15 cycles of burst were performed. Videos and images were acquired throughout the imaging procedure. Analysis was performed using VisualSonics imaging software (VisualSonics, Toronto, Canada).

Immunohistochemistry

The abdominal aorta was harvested following 4 weeks of Ang-II treatment or 3 days post-LPS injection, embedded in optimal cutting temperature compound (OCT; Sakura Finetek, Torrance, CA) and snapped frozen, and finally, 6-μm sections were obtained using a cryostat (Microm HM525 NX, Thermo Fisher Scientific, Waltham, MA). In order to determine VCAM-1 expression, multiple sections per animal were selected at random and underwent immunostaining using goat-anti-mouse VCAM-1 polyclonal antibody (Santa Cruz Biotechnology, Dallas, TX) following acetone and formalin fixation steps. The sections were then incubated with the appropriate biotinylated secondary antibody (Vector Laboratories, Burlingame, CA), and expression was determined via DDAB substrate (Vector Laboratories, Burlingame, CA). All relevant controls were performed. Sections of abdominal aorta were also stained for fibrin using MSB. Thawed sections were treated with Weigert's iron hematoxylin (Sigma-Aldrich, MO), incubated with 96% ethanol, and stained with Picric Orange G solution (EMS, PA). Sections were then further stained with Brilliant Crystal Scarlet 6R (Sigma-Aldrich, St. Louis, MO), and fibrin was differentiated using 1% phosphotungstic acid (EMS, Hatfield, PA). Finally, sections were stained with Aniline Blue solution (EMS, Hatfield, PA), rinsed in 1% acetic acid, dehydrated in 100% ethanol, cleared in xylene, and mounted using Depex mounting medium (Labchem, Zelienople, PA). Sections were rinsed in dH₂O between each step. For this MSB trichrome stain, erythrocytes, fibrin, and collagen are represented by orange, bright red, and blue, respectively. Sections were imaged using microscopy.

Microscopy

In vivo experiments were visualized with an IX81 Olympus microscope (Olympus, Tokyo, Japan) and Cell[^]P 1692 (ANALYSIS Image Processing) software, using bright field with a 20× objective and the tetramethylrhodamine (TRITC) fluorescence channel. Fluorescence was quantified using ImageJ software. Histological sections were visualized with an Olympus BX050F-3 microscope (Olympus, Tokyo, Japan) and CellSens software. All microscopy experiments were performed at ambient temperature.

Statistical Analysis

Unless otherwise specified, data are expressed as mean ± SD. Analyses containing 2 groups were analyzed with the Student's t test. All analyses containing more than two groups were analyzed with one-way ANOVA with repeated measures (if equal numbers)

or ordinary (if unequal numbers), comparing all groups with one another, corrected by post hoc Bonferroni analysis, and the corrected p values are given. Statistical analyses were performed using Graphpad Prism 6.0.

SUPPLEMENTAL INFORMATION

Supplemental Information includes three figures and three movies and can be found with this article online at <https://doi.org/10.1016/j.ymthe.2018.02.010>.

AUTHOR CONTRIBUTIONS

X.W. and K.P. conceived and designed the research. X.W., A.K.S., J.D.H., A.L.L., M.-K.A., J.P., B.L., Y.Y., M.W., E.Y., and Y.-C.C. performed the experiments. X.W., A.K.S., J.D.H., J.P., and K.P. analyzed the data. X.W., A.K.S., and K.P. wrote the manuscript.

CONFLICTS OF INTEREST

The authors have declared that no competing interests exist.

ACKNOWLEDGMENTS

The study was supported by the National Health and Medical Research Council (NHMRC) of Australia GNT1079492 and GNT1069492 and the Sir Edward Dunlop Medical Research Foundation Project Grant. X.W. and Y.-C.C. are supported by National Heart Foundation (NHF) Postdoctoral Fellowships and the NHF Paul Korner Innovation Awards. A.K.S. was supported by the NHF Australian Indigenous Scholarship. M.W. was supported by a German Research Foundation (DFG) Fellowship. K.P. was supported by a NHMRC Principal Research Fellowship.

REFERENCES

- Davis, F.M., Rateri, D.L., and Daugherty, A. (2015). Abdominal aortic aneurysm: novel mechanisms and therapies. *Curr. Opin. Cardiol.* *30*, 566–573.
- Golledge, J., Norman, P.E., Murphy, M.P., and Dalman, R.L. (2017). Challenges and opportunities in limiting abdominal aortic aneurysm growth. *J. Vasc. Surg.* *65*, 225–233.
- Peter, K., Nawroth, P., Conradt, C., Nordt, T., Weiss, T., Boehme, M., Wunsch, A., Allenberg, J., Kübler, W., and Bode, C. (1997). Circulating vascular cell adhesion molecule-1 correlates with the extent of human atherosclerosis in contrast to circulating intercellular adhesion molecule-1, E-selectin, P-selectin, and thrombomodulin. *Arterioscler. Thromb. Vasc. Biol.* *17*, 505–512.
- Siasos, G., Mourouzis, K., Oikonomou, E., Tsalamandris, S., Tsigkou, V., Vlasis, K., Vavuranakis, M., Zografos, T., Dimitropoulos, S., Papaioannou, T.G., et al. (2015). The role of endothelial dysfunction in aortic aneurysms. *Curr. Pharm. Des.* *21*, 4016–4034.
- Harris, T.A., Yamakuchi, M., Ferlito, M., Mendell, J.T., and Lowenstein, C.J. (2008). MicroRNA-126 regulates endothelial expression of vascular cell adhesion molecule 1. *Proc. Natl. Acad. Sci. USA* *105*, 1516–1521.
- Wang, S., Aurora, A.B., Johnson, B.A., Qi, X., McAnally, J., Hill, J.A., Richardson, J.A., Bassel-Duby, R., and Olson, E.N. (2008). The endothelial-specific microRNA miR-126 governs vascular integrity and angiogenesis. *Dev. Cell* *15*, 261–271.
- Fish, J.E., Santoro, M.M., Morton, S.U., Yu, S., Yeh, R.-F., Wythe, J.D., Ivey, K.N., Bruneau, B.G., Stainier, D.Y., and Srivastava, D. (2008). miR-126 regulates angiogenic signaling and vascular integrity. *Dev. Cell* *15*, 272–284.
- Schober, A., Nazari-Jahantigh, M., Wei, Y., Bidzhekov, K., Gremse, F., Grommes, J., Megens, R.T., Heyll, K., Noels, H., Hristov, M., et al. (2014). MicroRNA-126-5p promotes endothelial proliferation and limits atherosclerosis by suppressing Dlk1. *Nat. Med.* *20*, 368–376.
- Rupaimoole, R., and Slack, F.J. (2017). MicroRNA therapeutics: towards a new era for the management of cancer and other diseases. *Nat. Rev. Drug Discov.* *16*, 203–222.
- Wang, X., Gkanatsas, Y., Palasubramaniam, J., Hohmann, J.D., Chen, Y.C., Lim, B., Hagemeyer, C.E., and Peter, K. (2016). Thrombus-targeted theranostic microbubbles: A new technology towards concurrent rapid ultrasound diagnosis and bleeding-free fibrinolytic treatment of thrombosis. *Theranostics* *6*, 726–738.
- Wang, X., and Peter, K. (2017). Molecular imaging of atherothrombotic diseases: Seeing is believing. *Arterioscler. Thromb. Vasc. Biol.* *37*, 1029–1040.
- Moran, C.S., Biros, E., Krishna, S.M., Wang, Y., Tikellis, C., Morton, S.K., Moxon, J.V., Cooper, M.E., Norman, P.E., Burrell, L.M., et al. (2017). Resveratrol inhibits growth of experimental abdominal aortic aneurysm associated with upregulation of angiotensin-converting enzyme 2. *Arterioscler. Thromb. Vasc. Biol.* *37*, 2195–2203.
- Gottstein, C., Wels, W., Ober, B., and Thorpe, P.E. (2001). Generation and characterization of recombinant vascular targeting agents from hybridoma cell lines. *Biotechniques* *30*, 190–194, 196, 198 passim.
- Wang, X., Hagemeyer, C.E., Hohmann, J.D., Leitner, E., Armstrong, P.C., Jia, F., Olschewski, M., Needles, A., Peter, K., and Ahrens, I. (2012). Novel single-chain antibody-targeted microbubbles for molecular ultrasound imaging of thrombosis: validation of a unique noninvasive method for rapid and sensitive detection of thrombi and monitoring of success or failure of thrombolysis in mice. *Circulation* *125*, 3117–3126.
- Kwekkeboom, R.F.J., Lei, Z., Bogaards, S.J.P., Aiazian, E., Kamp, O., Paulus, W.J., Sluijter, J.P., and Musters, R.J. (2015). Ultrasound and microbubble-induced local delivery of MicroRNA-based therapeutics. *Ultrasound Med. Biol.* *41*, 163–176.
- Hagemeyer, C.E., von Zur Muhlen, C., von Elverfeldt, D., and Peter, K. (2009). Single-chain antibodies as diagnostic tools and therapeutic agents. *Thromb. Haemost.* *101*, 1012–1019.
- Hohmann, J.D., Wang, X., Krajewski, S., Selan, C., Haller, C.A., Straub, A., Chaikof, E.L., Nandurkar, H.H., Hagemeyer, C.E., and Peter, K. (2013). Delayed targeting of CD39 to activated platelet GPIIb/IIIa via a single-chain antibody: breaking the link between antithrombotic potency and bleeding? *Blood* *121*, 3067–3075.
- Hagemeyer, C.E., Alt, K., Johnston, A.P.R., Such, G.K., Ta, H.T., Leung, M.K.M., Prabhu, S., Wang, X., Caruso, F., and Peter, K. (2015). Particle generation, functionalization and sortase A-mediated modification with targeting of single-chain antibodies for diagnostic and therapeutic use. *Nat. Protoc.* *10*, 90–105.
- von Elverfeldt, D., Maier, A., Duerschmied, D., Braig, M., Witsch, T., Wang, X., Mauler, M., Neudorfer, I., Menza, M., Idzko, M., et al. (2014). Dual-contrast molecular imaging allows noninvasive characterization of myocardial ischemia/reperfusion injury after coronary vessel occlusion in mice by magnetic resonance imaging. *Circulation* *130*, 676–687.
- Lim, B., Yao, Y., Huang, A.L.-I., Yap, M.L., Flierl, U., Palasubramaniam, J., Zaldivia, M.T.K., Wang, X., and Peter, K. (2017). A unique recombinant fluorochrome targeting activated platelets allows in vivo detection of arterial thrombosis and pulmonary embolism using a novel three-dimensional fluorescence emission computed tomography (FLECT) technology. *Theranostics* *7*, 1047–1061.
- Yap, M.L., McFadyen, J.D., Wang, X., Zia, N.A., Hohmann, J.D., Ziegler, M., Yao, Y., Pham, A., Harris, M., Donnelly, P.S., et al. (2017). Targeting activated platelets: a unique and potentially universal approach for cancer imaging. *Theranostics* *7*, 2565–2574.
- Wang, X., Palasubramaniam, J., Gkanatsas, Y., Hohmann, J.D., Westein, E., Kanojia, R., Alt, K., Huang, D., Jia, F., Ahrens, I., et al. (2014). Towards effective and safe thrombolysis and thromboprophylaxis: preclinical testing of a novel antibody-targeted recombinant plasminogen activator directed against activated platelets. *Circ. Res.* *114*, 1083–1093.
- Ziegler, M., Hohmann, J.D., Searle, A.K., Abraham, M.-K., Nandurkar, H.H., Wang, X., and Peter, K. (2018). A single-chain antibody-CD39 fusion protein targeting activated platelets protects from cardiac ischaemia/reperfusion injury. *Eur. Heart J.* *39*, 111–116.
- Ziegler, M., Wang, X., Lim, B., Leitner, E., Klingberg, F., Ching, V., Yao, Y., Huang, D., Gao, X.M., Kiriazis, H., et al. (2017). Platelet-targeted delivery of peripheral blood mononuclear cells to the ischemic heart restores cardiac function after ischemia-reperfusion injury. *Theranostics* *7*, 3192–3206.

25. Schober, A., Nazari-Jahantigh, M., and Weber, C. (2015). MicroRNA-mediated mechanisms of the cellular stress response in atherosclerosis. *Nat. Rev. Cardiol.* *12*, 361–374.
26. Diehl, P., Fricke, A., Sander, L., Stamm, J., Bassler, N., Htun, N., Ziemann, M., Helbing, T., El-Osta, A., Jowett, J.B., and Peter, K. (2012). Microparticles: major transport vehicles for distinct microRNAs in circulation. *Cardiovasc. Res.* *93*, 633–644.
27. Zhang, W., Shang, T., Huang, C., Yu, T., Liu, C., Qiao, T., Huang, D., Liu, Z., and Liu, C. (2015). Plasma microRNAs serve as potential biomarkers for abdominal aortic aneurysm. *Clin. Biochem.* *48*, 988–992.
28. Wei, Y., Nazari-Jahantigh, M., Neth, P., Weber, C., and Schober, A. (2013). MicroRNA-126, -145, and -155: a therapeutic triad in atherosclerosis? *Arterioscler. Thromb. Vasc. Biol.* *33*, 449–454.
29. Kin, K., Miyagawa, S., Fukushima, S., Shirakawa, Y., Torikai, K., Shimamura, K., Daimon, T., Kawahara, Y., Kuratani, T., and Sawa, Y. (2012). Tissue- and plasma-specific microRNA signatures for atherosclerotic abdominal aortic aneurysm. *J. Am. Heart Assoc.* *1*, e000745.
30. Maegdefessel, L., Azuma, J., Toh, R., Deng, A., Merk, D.R., Raiesdana, A., Leeper, N.J., Raaz, U., Schoelmerich, A.M., McConnell, M.V., et al. (2012). MicroRNA-21 blocks abdominal aortic aneurysm development and nicotine-augmented expansion. *Sci. Transl. Med.* *4*, 122ra22.
31. Maegdefessel, L., Azuma, J., Toh, R., Merk, D.R., Deng, A., Chin, J.T., Raaz, U., Schoelmerich, A.M., Raiesdana, A., Leeper, N.J., et al. (2012). Inhibition of microRNA-29b reduces murine abdominal aortic aneurysm development. *J. Clin. Invest.* *122*, 497–506.
32. Di Gregoli, K., Mohamad Anuar, N.N., Bianco, R., White, S.J., Newby, A.C., George, S.J., and Johnson, J.L. (2017). MicroRNA-181b controls atherosclerosis and aneurysms through regulation of TIMP-3 and elastin. *Circ. Res.* *120*, 49–65.
33. Kim, C.W., Kumar, S., Son, D.J., Jang, I.-H., Griendling, K.K., and Jo, H. (2014). Prevention of abdominal aortic aneurysm by anti-microRNA-712 or anti-microRNA-205 in angiotensin II-infused mice. *Arterioscler. Thromb. Vasc. Biol.* *34*, 1412–1421.
34. Zernecke, A., Bidzhikov, K., Noels, H., Shagdarsuren, E., Gan, L., Denecke, B., Hristov, M., Köppel, T., Jahantigh, M.N., Lutgens, E., et al. (2009). Delivery of microRNA-126 by apoptotic bodies induces CXCL12-dependent vascular protection. *Sci. Signal.* *2*, ra81.